Estimation of Snow Mass Information via Assimilation of C-Band Synthetic Aperture Radar Backscatter Observations Into an Advanced Land Surface Model

Jongmin Park [ID], Barton A. Forman [ID], and Sujay V. Kumar

Abstract—This study assimilated Sentinel-1 C-band backscatter observations over snow-covered terrain into the Noah-Multiparameterization land surface model using support vector machine (SVM) regression and an ensemble Kalman filter to improve the modeled terrestrial snow mass estimates. The data assimilation (DA) experiment was conducted across Western Colorado from September 2016 to August 2017. As part of the DA experiments, the impact of a rule-based update was evaluated by comparing snow water equivalent (SWE) estimates via DA (with [DA_{v1}] and without [DA_{v2}] the rule-based update) against SNOTEL SWE measurements. Results confirmed that rule-based update helped minimize SVM controllability issues, and in turn, improved the accuracy of SWE estimates relative to both open loop (OL) and DA_{v2}. Comparison of SWE estimates from Sentinel-1 DA_{v1} against SNOTEL SWE revealed that 75% of stations showed improvements in bias and correlation coefficient relative to the OL. Assimilated SWE estimates also showed statistical improvements during both the snow accumulation and snow ablation periods. However, unbiased root mean square error showed a slight increase during the snow ablation period due to the large variability in the electromagnetic response of C-band backscatter over deep and/or wet snow. Improvement of the SWE estimates also resulted in improving river discharge estimates compared to *in situ* measurements. River discharge using Sentinel-1 DA_{v1} improved the Nash–Sutcliffe efficiency at all available stations. These results suggest that physically constrained SVM can serve as an efficient observation operator for snow mass DA through explicit consideration of the first-order C-band scattering mechanisms over different terrestrial snow conditions.

Index Terms—Data assimilation (DA), land surface model (LSM), NASA land information system (LIS), support vector machine (SVM), synthetic aperture radar (SAR).

Jongmin Park is with the Universities Space Research Association, Columbia, MD 21046 USA, and also with the NASA Goddard Space Flight Center, Greenbelt, MD 20771 USA (e-mail: jongmin.park@nasa.gov).

Barton A. Forman is with the Department of Civil and Environmental Engineering, University of Maryland, College Park, MD 20742 USA (e-mail: baforman@umd.edu).

Sujay V. Kumar is with the Hydrological Science Lab, NASA Goddard Space Flight Center, Greenbelt, MD 20771 USA (e-mail: sujay.v.kumar@nasa.gov).

I. INTRODUCTION

QUANTIFYING the snow mass [e.g., snow water equivalent (SWE) and snow depth] across the globe is essential for understanding the terrestrial water and energy cycles as well as in aid of efficient water resources management efforts [1]–[3]. However, conventional, ground-based measurements of snow mass have limitations in terms of capturing the spatial and temporal dynamics of terrestrial snow [4], [5]. Land surface models (LSMs) are another available option to estimate spatio-temporal variations of snow mass over large regions, but LSMs have their own inherent uncertainties associated with model structure, parameter characterization, initial conditions, and meteorological boundary conditions [6], [7]. These limitations in ground-based measurements and LSMs motivate the application of remotely sensed observations from space-borne instruments as an alternative to characterize terrestrial snow mass across regional and continental scales.

In recent decades, passive microwave (PMW) and active microwave remote sensing instruments have been utilized for monitoring terrestrial snow. Efforts at retrieving snow mass using PMW radiometers have been pursued since the 1980 s by leveraging the quasi-linear relationship between snow mass and brightness temperature, T_b [8]–[10]. However, sensor limitations in areas of dense vegetation, deep snow, or wet snow coupled with the coarse spatial resolution of PMW radiometry limit its application in mountainous terrain, where snow is often found [11], [12].

Active microwave remote sensing, most notably space-borne synthetic aperture radar (SAR), is an alternative approach to PMW radiometry in retrieving snow mass. Backscatter measured over snow-covered terrain is largely influenced by snow wetness based on the underlying, first-order physics of large differences in the dielectric constants between ice and water [13]. The utilization of SAR imagery offers advantages in terms of its all-weather capability, relatively fine spatial resolution (compared to PMW radiometry), and multipolarization capabilities [14]. Previous research utilized Spaceborne Imaging Radar (SIR)-C/X-SAR [15], European Remote Sensing satellite (ERS)-1/2 [16], Envisat [17], RADARSAT [18], and Sentinel-1 [2], [19] in order to retrieve terrestrial SWE and snow depth. However, complex relationships between backscatter and

snowpack properties (e.g., snow grain size, snow density), as well as the influence of the overlying vegetation and underlying soil limits the efficacy of backscatter to estimate snow mass [19], [20].

As a complement to LSMs and remotely sensed observations, data assimilation (DA) offers the potential of obtaining optimal estimates of geophysical variables (e.g., snow mass) that are superior to either the remote sensing retrievals or the LSM-only estimates [21]. For example, snow cover information (i.e., snow cover fraction [SCF] and snow cover area [SCA]) retrieved from optical imagery has been used to improve SWE and snow depth estimates in LSMs [22]–[26]. Updated (a.k.a., *a posteriori*) SWE using SCA and SCF DA yielded slight improvements when compared with the open loop (OL; model-only run) across snow-covered terrain. However, studies also have shown disadvantageous impacts from DA when mapping SCA or SCF into SWE space by using a snow depletion curve [22], [23]. Furthermore, when the area is completely snow-covered, sequential assimilation of SCA provides no additional information to SWE via DA.

Another option to update snow mass is to utilize the T_b observations (or spectral difference, ΔT_b) observed from the advanced microwave scanning radiometer for EOS (AMSR-E) [5], [27], [28], AMSR2 [29], or the special sensor microwave/Imager (SSM/I) [30], [31]. Snow mass estimates from PMW DA showed slight improvements over the OL in terms of reduced bias and RMSE when compared against ground-based measurements [5], [29]. However, others have shown that the assimilation of PMW T_b (or spectral difference, ΔT_b) resulted in increased uncertainties in snow mass estimates. More specifically, biases in the PMW T_b retrievals in regions with relatively deep snow, wet snow, dense forest, or inland water bodies, where PMW T_b typically exhibits biases were correspondingly propagated into the DA, and in turn, resulted in increased uncertainty in the snow mass estimates [5], [28], [29], [32].

In the case of active microwave observations, there are relatively few studies employing SAR observations into a DA framework to improve snowpack estimates. Luojus *et al.* [33] utilized meteorological variables (e.g., cloud cover, wind speed, and air temperature) measured from ground-based stations for use in a simple rule-based approach to update RADARSAT-derived SCA that was calculated using the Helsinki University of Technology (TKK) SCA estimation algorithm. The experiment was conducted over the boreal forest zone in Finland for the time period of 2004–2006. Evaluation of the updated SCA estimates showed better agreement with Moderate Resolution Imaging Spectroradiometer (MODIS) snow cover retrievals than the SCA estimates without the rule-based update. Analogously, Phan *et al.* [34] assimilated TerraSAR-X observations as well as computed backscatter estimates from an electromagnetic backscattering model, which is generally based on the dense media radiative transfer algorithm, into a one-dimensional (1-D) Crocus snowpack model in order to improve snow stratigraphic profiles on the Argentiére glacier during the winter of 2008–2009. Results indicated that assimilation of X-band SAR observations into Crocus resulted in a better representation of

the electromagnetic response in each snow layer as well as the overall snowpack profile.

The study presented here assimilates C-band SAR backscatter observations collected by Sentinel-1 into the Noah-multiparametrization (Noah-MP) LSM to improve the accuracy of the terrestrial snow mass. Among the various components in a DA framework, the observation operator is regarded as one of the key parts [35], which links the system state vector with the observations. Typically, a physical-based snow emission model or radiative transfer model is used as the observation operator. Alternatively, more recent research has explored the use of machine learning (ML) algorithms for use as an observation operator given the algorithm's capability at capturing the spatio-temporal variability of the satellite observations [5], [36]–[39]. Most recently, Park *et al.* [40] investigated the utilization of physically constrained support vector machine (SVM) regression to reproduce C-band backscatter over snow-covered land. The research presented here is a first attempt to merge C-band backscatter observations collected by Sentinel-1 into an advanced LSM using SVM regression as the observation operator. The main scientific inquiry addressed in this study is whether integration of C-band backscatter observations into a LSM using a ML algorithm and an ensemble-based DA framework results in better characterization of terrestrial snow mass estimates. More specifically, the article addresses the following scientific questions.

1) Can a physically constrained ML algorithm that implicitly represents the physical properties of snow serve as an effective forward modeling approach in the context of C-band SAR snow assimilation?

2) Does the assimilation of Sentinel-1 backscatter observations into the Noah-MP LSM add value in the context of improving the accuracy (and reducing the uncertainty) of modeled snow mass estimates?

3) Does the improvement in snow mass estimates via assimilation translate into improvements in river discharge estimates?

II. STUDY AREA AND DATASETS

A. Study Area

The study domain selected here is Western Colorado, where 12 subbasins are entirely or partially located within the study area (see Fig. 1). The subbasins located in the western part of the study domain are within the Upper Colorado River basin, which is a primary water supply resource to more than 30 million people [41]. The Upper Colorado basin has an average annual precipitation and temperature of 100 cm and 6 °C, respectively [42]. The eastern part of the study domain contains parts of the Missouri River basin in the north and part of the Arkansas-White-Red River basin in the south. These regions receive an annual average precipitation that ranges from 60 cm to 150 cm with 40–70% in the form of snow during the winter. The study domain also contains several major tributaries of the Colorado River (e.g., Gunnison River, San Juan River, Little Snake River, and Yampa River), which supplies freshwater resources
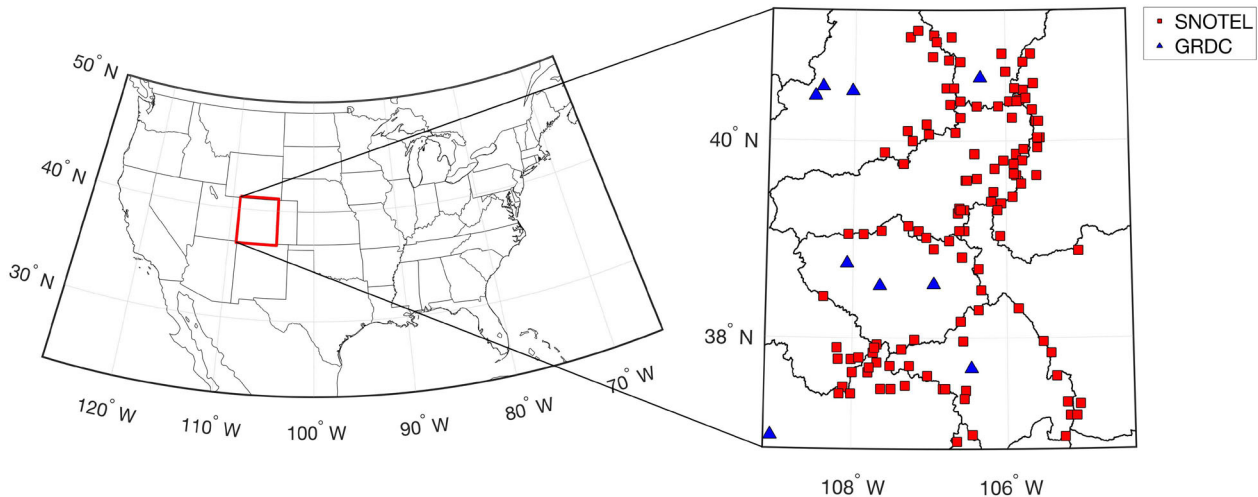
Fig. 1.　Geographic maps of the study domain, including the location of SNOTEL snow measurements and GRDC runoff measurements. The black lines in the right-most figure represent the boundary lines of individual subbasins (based on Hydrological Unit Code level 4) provided by the USGS.[1]

to more than 40 million people in adjacent U.S. states as well as parts of Mexico [43]. Snowpack that melts during the springtime in the high elevations of the Rocky Mountains contributes to approximately 70% of the annual streamflow across the study domain [41], [44]. In addition, southern portions of the Rocky Mountains are located within the study domain, including the San Juan, Rio Grande, and Grand Mesa national forests.

B. Ground-Based Measurements

Evaluation of snow mass estimates (i.e., SWE and snow depth) from both the model-alone simulation (OL) and the DA simulation were conducted via comparison to SWE from the SNOwpack Telemetry (SNOTEL) network. SNOTEL is a ground-based measurement network operated by the U.S. Department of Agriculture National Resources Conservation Services (NRCS;[2] and provides SWE, snow depth, precipitation, and air temperature measurements. In this study, SWE measurements during the validation period (e.g., September 2016–August 2017) were collected from 112 stations located across the study domain (see Fig. 1). The average elevation for the selected sites was 3071 m with the lowest elevation being 2268 m (Battle Mountain; WY317) and the highest elevation being 3542 m (Sargents Mesa; CO 1128).

In addition to the SNOTEL stations, unnaturalized, daily river discharge measurements obtained from the Global Runoff Data Center (GRDC;[3] were utilized to evaluate the model-driven discharge estimates from both the OL and DA. As shown in Fig. 1, nine stations are located within the study domain while one GRDC station was excluded from the analysis as it does not have available measurements during the study period. The range of mean annual streamflow from the selected stations is from 12.2 to 198.8 m³/s with a mean station elevation of

1770 m. This comparison allows us to examine the hypothesis that updated snow mass estimates will result in improvements of model-based runoff estimates in terms of timing and volumetric discharge. Note that these stations are not affected by nearby reservoirs.

C. Sentinel-1 Backscatter Observations

C-band backscatter observations from Sentinel-1, a constellation consisting of Sentinel-1 A (launched in April 2014) and Sentinel-1B (launched in April 2016) operated by the European Space Agency, are utilized in this study [45]. C-band SAR sensors with a central frequency of 5.407 GHz are onboard both Sentinel-1 A and -1B and share the same orbital plane with a 180° phase difference [46]. Each Sentinel-1 platform has a sun-synchronous orbit with a 98.18° inclination angle. The revisit frequency of each Sentinel-1 satellite is designed as 12-days, which leads to achieving a 6-day revisit frequency between the constellation of two satellites. However, Sentinel-1 observations over the study domain showed an irregular overpass frequency prior to early 2017 due to the evolving data acquisition scenario.[4]

Sentinel-1 provides different types of datasets depending on the measurement mode (e.g., Strip-map, Interferometric Wide swath [IW], Extra Wide swath, and Wave [WV] mode) as well as different processing levels (e.g., single look complex [SLC], ground range detected [GRD], and ocean [OCN]) [46]. Among the different types of products, the Sentinel-1 IW GRD product is used here because the primary objective is to estimate terrestrial snow mass information. In addition, this article primarily focuses on the use of backscatter observations from the ascending overpasses (measured around 6 P.M. local time) as C-band backscatter exhibited a more sensitive electromagnetic response (e.g., large absorption and reflection) associated with snow liquid water content during wet snow conditions [40].

---

[1][Online]. Available: https://water.usgs.gov/GIS/huc.html

[2][Online]. Available: https://www.wcc.nrcs.usda.gov/snow/

[3][Online]. Available: https://www.bafg.de/GRDC/EN/Home/homepage_node.html

[4][Online]. Available: https://sentinel.esa.int/web/sentinel/missions/sentinel-1/observation-scenario

In general, the efficacy of SAR backscatter observations is limited by a number of uncertainties, including geometric distortions (e.g., foreshortening and overlying) as well as thermal and speckle noise [47]. In order to minimize these deleterious effects, preprocessing of Sentinel-1 observations employed the methods of Lievens *et al.* [2] using the Google Earth Engine. Furthermore, preprocessed Sentinel-1 imagery was resampled onto a 0.01° equidistant cylindrical grid to coincide with the spatial resolution of geophysical estimates from the Noah-MP lLSM, which is discussed in the following section.

D. NASA Land Information System

The NASA Land Information System (LIS) is an open source software framework developed at the Goddard Space Flight Center.[5] LIS contains various components including advanced LSMs, different types of observation readers (e.g., ground and satellite observations), DA algorithms, and high-performance computing routines [48]. Among the different LSMs within LIS, the Noah-multiparameterization version 3.6 (Noah-MP; Niu *et al.* [49]) model was chosen for use in this study.

The basic framework of Noah-MP follows that of the Noah LSM with the additional augmentation of multiple parameterization options in order to improve the representation of land-atmosphere interactions [49]. In terms of terrestrial snow, Noah-MP contains a physically based snow model with three snow layers and improved snow albedo schemes, which results in better representation of snow mass estimates and snowmelt timing as compared to the Noah LSM [49], [50]. For the parameterization of snow surface albedo, the biosphere-atmosphere transfer scheme (BATS; Yang *et al.* [51]) was employed in this study. In addition, routines introduced in Jordan [52] were utilized for the purpose of partitioning liquid versus solid rainfall from the total precipitation. Details of the specific parameterization approaches used in Noah-MP follows the approach introduced in Kwon *et al.* [39].

III. EXPERIMENTAL SETUP

A. Ensemble OL

Before running each simulation, initial conditions of soil moisture and shallow groundwater for the model were established during a spin-up period from January 1980 to May 2015 using a single (nominal) replicate. Next, a 20-member ensemble of model realizations was computed using an additional model run between May 2015 and August 2016 based on perturbed meteorological fields from the Modern-Era Retrospective analysis for Research and Application, version 2 (MERRA-2; Gelaro *et al.* [53]) and Tropical Rainfall Measuring Mission (TRMM; Huffman *et al.* [54]) products that were used as boundary conditions.

Perturbation of model forcings is one key aspect of the OL (and DA) simulations that implicitly characterizes the uncertainty in the mass and energy boundary conditions, and hence, the resulting snowpack in the ensemble replicates of the LSM.

[5][Online]. Available: https://lis.gsfc.nasa.gov/

Details of the perturbation approach follow that employed in Kwon *et al.* [39] and Reichle *et al.* [21]. Selected parameters for perturbation include the radiation components (i.e., downwelling shortwave and downwelling longwave radiation), near-surface air temperature, and precipitation. An overview of the perturbation parameters is summarized in Table I. Throughout all four forcings, a first-order, autoregressive model temporal correlation of one day was used. In the case of shortwave radiation and precipitation, these parameters were perturbed using additive, zero-mean Gaussian distributions while multiplicative, log-normal distributions with a mean of one were utilized to perturb longwave radiation and near-surface air temperature.

With the established ensemble of initial conditions, Noah-MP was then applied in the experiments using model-only (a.k.a., OL) and DA techniques from September 2016 to August 2017. Experiments were conducted on a 0.01° equidistant cylindrical grid and outputs were generated at a daily time step that was aggregated up from the 15-min model time step.

B. 1-D Ensemble Kalman Filter

This study employed a 1-D Ensemble Kalman Filter (EnKF; Evensen [55]) to integrate C-band backscatter observations into the Noah-MP LSM. One main advantage of the EnKF is that it does not require linear models, which leads to its widespread application in hydrologic studies including soil moisture [56]–[58], snow mass [5], [59]–[61], and streamflow [28], [62], [63].

The basic idea of an EnKF is the implementation of a Monte Carlo approach using an ensemble of realizations that implicitly contains the model error covariance structure along with the boundary condition errors [35]. As part of the EnKF routine, ensemble replicates are propagated in time after, which updates of model states are determined based on the mean and standard deviation of the ensemble replicates that approximate the state distribution. During the model propagation step, the *a priori* state vector at time step t, y_t^{i-}, is calculated as a function of *a posteriori* model state vector at time step $t-1$, y_{t-1}^{i+}, forcings, $u_{i,t-1}$, and additive model error, α_i, which can be written as

$$y_t^{i-} = f(y_{t-1}^{i+}, u_{i,t-1}, \alpha_i) \ \forall \ i \in [1, 2, \ldots N_r]$$

$$\text{with } y(t = t_0) = y_0 \qquad (1)$$

where i represents a single replicate that is propagated with the geophysical (i.e., Noah-MP LSM), $f(\cdot)$, and N_r represents the number of the ensemble replicates. In this study, $N_r=20$ ensemble replicates was selected based on Kwon *et al.* [39]. After the propagation step, the EnKF uses an update equation when an observation is available as follows:

$$y_t^{i+} = y_t^{i-} + K_t[(Z_t + \epsilon^i) - M(y_t^{i-})] \qquad (2)$$

where y_t^{i-} and y_t^{i+} indicate the *a priori* and *a posteriori* model state of the ith ensemble at time step t, respectively. Z_t is the Sentinel-1 backscatter observation at a given location at the measurement time t that is perturbed with measurement error, ϵ^i, following a Gaussian error distribution of mean zero and observation error covariance, R. $M(y_t^{i-})$ is the backscatter estimate from the observation operator, $M(\cdot)$, which maps the geophyiscal model space into backscatter observation space. In

TABLE I
SUMMARY OF PERTURBATIONS APPLIED TO THE METEOROLOGICAL BOUNDARY CONDITIONS USED IN BOTH THE OL AND
DA EXPERIMENTS

Boundary Conditions	Error Type	Standard Deviation	AR(1)	Cross Correlation			
				SW	LW	P	T_a
Shortwave Radiation (SW)	M	0.5	1 day	1	-0.5	-0.8	0.3
Longwave Radiation (LW)	A	50 Wm^{-2}	1 day	-0.5	1	0.5	0.6
Rainfall Rate (P)	M	0.5	1 day	-0.8	0.5	1	-0.1
Air Temperature (T_a)	A	1 K	1 day	0.3	0.6	-0.1	1

Note: M and a represent multiplicative and additive, respectively. AR(1) represents the first-order, autoregressive temporal correlation. Air temperature is for the near-surface at approximately 2 m above the ground surface.

this study, SVM regression serves as $M(\cdot)$ (see Section III-C for details). K_t is the Kalman gain matrix, which is a relative measure of the observation error and the model error that determines the magnitude and sign of the update. K_t can be computed as

$$K_t = \text{Cov}(y_t^{i-}, M(y_t^{i-}))[\text{Cov}(M(y_t^{i-}), M(y_t^{i-})) + R]^{-1} \quad (3)$$

where $\text{Cov}(y_t^{i-}, M(y_t^{i-}))$ represents the error cross-covariance between the *a priori* model estimates and estimated backscatter derived from the observation operator. $\text{Cov}(My_i^-, My_i^-)$ denotes the error (sample) covariance of the estimated backscatter derived from the observation operator. R is the time-invariant observation error covariance of the Sentinel-1 backscatter observations. Based on Lievens *et al.* [64], 0.3^2 dB^2 was selected as the error covariance for the Sentinel-1 backscatter observations.

C. ML Observation Operators

The main role of the observation operator, $M(\cdot)$, within the DA framework is to map the geophysical model states (e.g., SWE estimated from Noah-MP) into observation (i.e., C-band backscatter) space. Existing studies [36]–[39] demonstrate the ability of ML algorithms as an effective observation operator (instead of a radiative transfer model, e.g.) for snow mass assimilation. More specifically, Park *et al.* [40] revealed that physically constrained SVM regression developed over snow-covered terrain reasonably reproduced C-band backscatter observations when explicitly considering the difference in electromagnetic response during different snow conditions (e.g., wet snow versus dry snow).

Given the [1 × Q] input vector (n) that represents the geophysical variables from Noah-MP, the general solution to SVM regression can be written as

$$\begin{bmatrix} \hat{\sigma}_{VV} \\ \hat{\sigma}_{VH} \end{bmatrix} = f(x) = \sum_{i=1}^{P} (\alpha_i - \alpha_i^*) k(x_i, n) + \delta \quad (4)$$

where $\hat{\sigma}_{VV}$ and $\hat{\sigma}_{VH}$ denotes the predicted co- and cross-polarized backscatter from the well-trained SVM, respectively. Training matrix, x, contains the model input vectors, n, at the times of P training targets at a given pixel with a matrix size of [P × Q]. P and Q indicate the number of available training target sets and input datasets, respectively, within a given training window [65]. α_i and α_i^* denote the dual Lagrangian multipliers and δ represents the offset coefficients. Among the different kernel types, the Gaussian radial basis kernel function, $k(x_i, n) = \exp\{-\gamma||x_i - n||^2\}$, was selected for use in this study, where $||\cdot||$ represents the Euclidean norm. Solution of

Equation (4) was performed using the LIBSVM library [66], which is an open source, ML module provided by National Taiwan University. SVM training and prediction follows the procedure outlined in Park *et al.* [40] and is also summarized in the following section.

1) SVM Training and Prediction Procedure: Training targets include both copolarized, σ_{VV}, and cross-polarized, σ_{VH}, Sentinel-1 C-band backscatter observations over snow-covered terrain. In addition, binary (i.e., yes/no) snow cover retrievals from the interactive multisensor snow and Ice Mapping System (IMS) snow cover product from the National Oceanic and Atmospheric Administration/National Environmental Satellite, Data, and Information Service (NOAA/NESDIS) are used as a quality control agent during training. Backscatters at different polarizations were trained separately because of the different electromagnetic responses in σ_{VV} and σ_{VH} depending on the snow wetness [67]–[69]. For example, σ_{VV} exhibits relatively little variability associated with changing snow mass during the dry snow season because the relatively deep penetration depth of C-band radiation causes the total backscatter to be predominantly controlled by scattering at the snow-land interface [70] rather than volume scattering within the snowpack. However, an increase in liquid water content within the snowpack during wet snow conditions leads to more absorption of C-band photons that, in general, results in a significant reduction of σ_{VV} [2]. In the case of σ_{VH}, C-band photon scattering is more variable as it is more sensitive to multiple scatterings within the snowpack as compared to copolarized C-band radiation [71], [72].

During the SVM training phase, Sentinel-1 observations (both σ_{VV} and σ_{VH}) collected between April 2015 to August 2016 and September 2017 to August 2018 were selected for use. In order to implement a split-sampling procedure, Sentinel-1 observations from September 2016 to August 2017 were excluded from SVM training, and instead, were used during the validation procedure. Training at each individual grid cell used a fortnightly training period that included two weeks before and two weeks after the specific fortnight of interest [40]. This was done to better capture the snow seasonality while also reducing discontinuities between one fortnightly prediction period and the next [37].

In addition to the selection of the training targets, the optimal selection of input variables plays an important role in introducing appropriate physical constraints into the statistical learning process. Following the techniques outlined in Park *et al.* [40], four snow-related geophysical variables estimated from Noah

MP (i.e., SWE, snow density, snow liquid water, and top-layer snow temperature) were selected for this study. The selection of this particular set of input datasets was predicated on the C-band scattering mechanisms over snow-covered terrain as well as on the results of an extensive sensitivity analysis.

2) SVM Controllability Issues: In general, the controllability of a system is guaranteed if and only if changing physically plausible inputs to the system leads to a physically plausible change in system output [73]. Once the appropriate type and number of input datasets and training targets are established, the SVM-based DA framework, in general, is controllable. However, controllability issues sometimes arise when the trained SVM is required to make predictions based on inputs (scenarios) that were not witnessed during the training procedure. Unfortunately, as previously mentioned in Section II-C, irregular data acquisition before early-2017 influenced the number of available training datasets and can, at times, lead to the generation of an uncontrollable SVM-based observation operator that, at times, significantly degrades the accuracy of snow mass estimates via DA.

In order to minimize this controllability issue, a rule-based DA update was applied in this study. First, when considering the typical range of Sentinel-1 backscatter observations over snow-covered terrain (i.e., ranged from -30 to 0 dB in both σ_{VV} and σ_{VH}), assimilation was temporarily disabled when the predicted backscatter was outside of this specific range. Further, when the absolute deviation between predicted and observed backscatter was larger than an established threshold (i.e., 10 dB based on the findings of Park *et al.* [40]), the assimilation routine was temporarily disabled. These simple rules are intended to help mitigate issues related to a lack of SVM controllability that occurs infrequently, but has deleterious effects when it does occur.

3) HyMAP River Routing: The Hydrological Modeling and Analysis Platform (HyMAP; Getirana *et al.* [74]) is a flood routing scheme that simulates large-scale riverine flow dynamics (e.g., water level, discharge, and storage) in both the main river channel and the associated floodplains. HyMAP includes four modules prescribing time delays in: 1) surface discharge and baseflow, 2) interface between the stream and floodplain, 3) streamflow routing, and 4) open water surface evaporation [74], [75]. HyMAP has been successfully coupled to different LSMs and has been used to simulate runoff across the globe [74], [76]–[80]. In this study, HyMAP is coupled to Noah-MP within the LIS framework so that estimated runoff and baseflow from Noah-MP is routed using a kinematic wave approximation within a predefined river network and floodplain. A detailed description of HyMAP parameters schemes is provided in Getirana *et al.* [74].

4) Evaluation Metrics: For the evaluation of DA performance, SWE estimates from both the OL and Sentinel-1 DA, were compared against ground-based measurements as presented in Section II-B. Pearson correlation coefficient (R), bias, root mean square error (RMSE), and unbiased RMSE (ubRMSE) were used to quantitatively examine model performance. R is a measure of the agreement in temporal variation between the model estimates and ground-based measurements. Bias

represents the systematic error while RMSE accounts for both systematic and nonsystematic errors. In addition, unbiased RMSE (ubRMSE; Entekhabi *et al.* [81]) was also computed to focus on the nonsystemic error by first removing the bias from RMSE. These statistical metrics were computed as

$$R = \frac{\sum_{t=1}^{N_s}(\langle y_{\text{est},t}\rangle - \bar{y}_{\text{est},t})(y_{\text{meas},t} - \bar{y}_{\text{meas}})}{\sqrt{\sum_{t=1}^{N_s}(\langle y_{\text{est},t}\rangle - \langle \bar{y}_{\text{est}}\rangle)^2}\sqrt{\sum_{t=1}^{N_s}(y_{\text{meas},t} - \bar{y}_{\text{meas}})^2}} \tag{5}$$

$$\text{bias} = \frac{1}{N_s}\sum_{t=1}^{N_s}(\langle y_{\text{est},t}\rangle - y_{\text{meas},t}) \tag{6}$$

$$\text{ubRMSE} = \text{RMSE}^2 - \text{bias}^2 \tag{7}$$

where $\langle y_{\text{est},t}\rangle$ represents the ensemble mean of SWE estimates at time t obtained from either the OL or Sentinel-1 DA; $y_{\text{meas},t}$ denotes the ground-based SWE at time t; $\langle \bar{y}_{\text{est}}\rangle$ is the time-averaged ensemble mean of SWE estimates from the OL or Sentinel-1 DA; $\bar{y}_{\text{meas}}$ denotes the time-averaged SWE from the ground-based measurements; and N_s represents the total number of samples in time at a given location in space.

In addition to the above statistical metrics, Nash-Sutcliffe efficiency (NSE; Nash and Sutcliffe [82]), which is a widely used goodness-of-fit measures to evaluate model performance, is utilized in this study in order to evaluate river discharge estimates from the OL and Sentinel-1 DA simulation against the *in situ* GRDC measurements. NSE was calculated as

$$\text{NSE} = 1 - \frac{\sum_{t=1}^{N_s}(y_{\text{meas},t} - \langle y_{\text{est},t}\rangle)^2}{\sum_{t=1}^{N_s}(y_{\text{meas},t} - \langle y_{\text{est},t}\rangle)^2}. \tag{8}$$

In this study, utilization of NSE to evaluate river discharge estimates from both the OL and Sentinel-1 DA is a useful measure to assess whether the updated SWE estimates via Sentinel-1 DA resulted in improving the river discharge estimates in terms of both timing and volume.

IV. RESULTS AND DISCUSSION

A. Evaluation of SWE Against Ground-Based Measurements

Daily-averaged SWE estimates from both the OL and Sentinel-1 DA with the rule-based update presented in Section III-C2 (hereafter referred to as Sentinel-1 DA_{v1}) were compared against the SNOTEL SWE measurements from September 2016 to August 2017. Fig. 2 illustrates the temporal mean of R and bias and the corresponding improvements in statistical metrics at the SNOTEL stations when using Sentinel-1 DA_{v1}. In the case of OL, R ranged from -0.21 to 0.99 while R for Sentinel-1 DA_{v1} ranged from -0.18 to 0.99. Among all available SNOTEL stations, more than 90% yielded a statistically significant improvement in correlation, indicating that Sentinel-1 DA_{v1} resulted in better agreement in terms of seasonal variation with the SNOTEL SWE measurements relative to the OL simulation. Similar behavior was observed for bias in that Sentinel-1 DA_{v1} showed a smaller magnitude in bias than the OL [see Fig. 2(f)]. The bias in SWE estimated from the OL ranged from -0.55 to 0.11 m while the bias of SWE simulated from
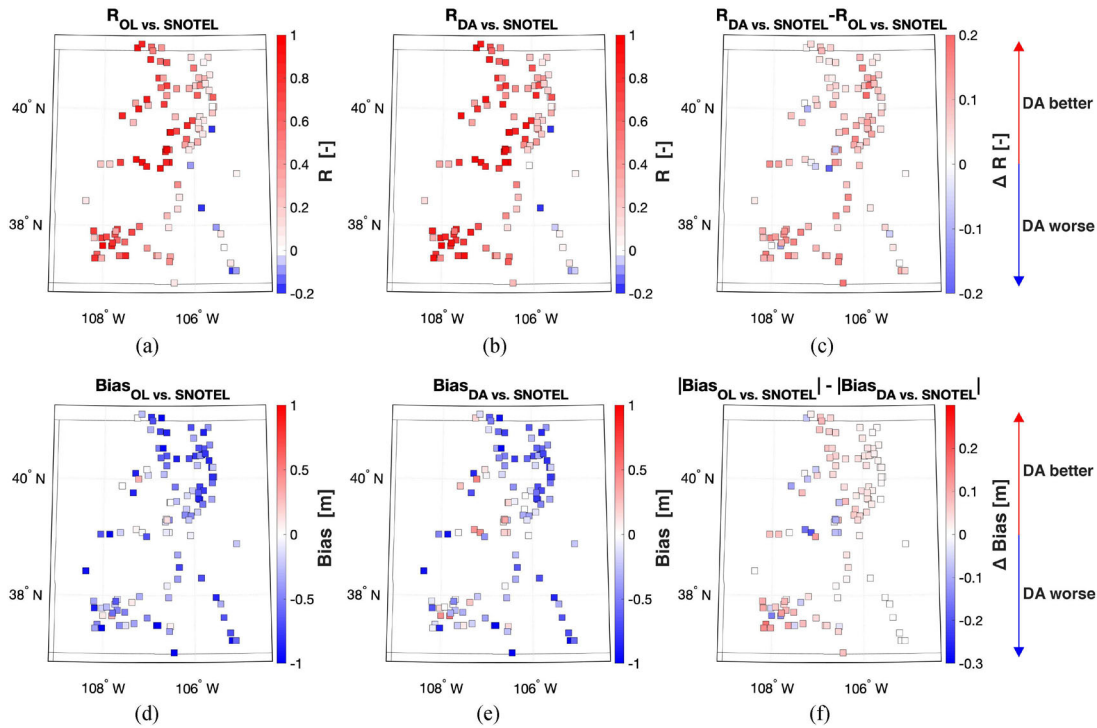
Fig. 2.   Spatial maps of correlation coefficient, R, (top row) and bias (bottom row) computed against the SNOTEL SWE measurements from September 2016 to August 2017. Left and middle columns represent the statistics of OL SWE and Sentinel-1 DA_{v1} (with rule-based update) SWE, respectively. The differences in R and differences in absolute bias are shown in (c) and (f), respectively. The red colors (positive values) in (c) and (f) suggests that Sentinel-1 DA_{v1} agrees better with SNOTEL SWE than does the OL. Oppositely, blue colors (negative values) indicate that the OL showed better agreement with SNOTEL SWE than did Sentinel-1 DA_{v1}.
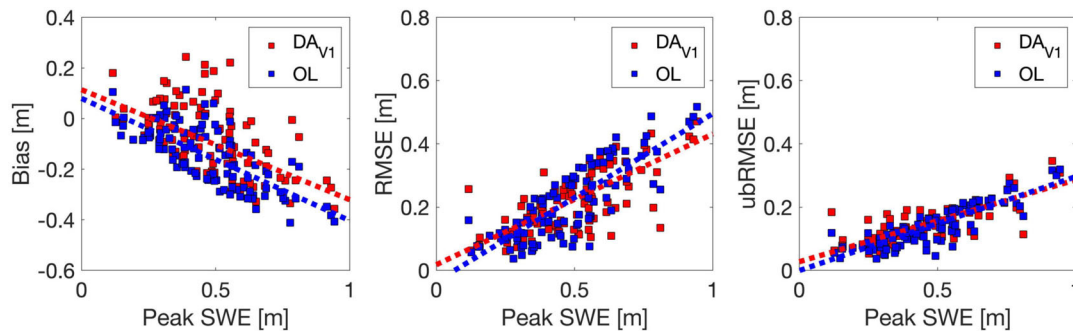
Fig. 3.   Scatter plots of bias, RMSE, and ubRMSE in accordance with peak SWE as observed by the SNOTEL stations. Note that the blue and red dots represent the OL and Sentinel-1 DA_{v1}, respectively.

Sentinel-1 DA_{v1} ranged between -0.49 to 0.24 m. In general, SWE estimates from Sentinel-1 DA_{v1} showed less bias than the OL at 84 SNOTEL stations (out of a total of 112) located within the study domain. Furthermore, results indicated that more than 80 SNOTEL stations (out of a total of 112) showed statistically significant improvements in terms of R, bias, and RMSE. Station-averaged bias for OL and Sentinel-1 DA_{v1} were revealed as -0.20 and -0.11 m, respectively. Station-averaged RMSE also showed a slight decrease from 0.27 (OL) to 0.25 m (Sentinel-1 DA_{v1}).

According to Fig. 2(d) and (e), most of the bias in the OL and DA simulations was negative across the study domain. One of the main reasons for the discrepancy between simulated and measured SWE can be explained through errors in the model

boundary conditions (i.e., precipitation) or due to the spatial scale mismatch between the model and the measurements. That is, ground-based measurements have a spatial footprint of $\sim 1\,m^2$ while modeled SWE estimates from both the OL and Sentinel-1 DA_{v1} have a spatial footprint of $\sim 10^6\,m^2$. Furthermore, the bias in SWE estimates from both the OL and Sentinel-1 DA_{v1} is increasingly negative with an increase in the amount of peak SWE (see Fig. 3). The increase in SWE uncertainty with higher mean SWE can also be partially explained by errors in the modeled snow albedo. Snow albedo is a first-order control on the partitioning of available energy at the surface, and in turn, influences the amount of snowmelt [83]. Kumar *et al.* [84] assimilated MODIS albedo retrievals into the Noah-MP LSM over the continental U.S. The results showed that the model-only

TABLE II
DOMAIN-AVERAGED STATISTICS OF SWE ESTIMATED FROM THE OL AND
SENTINEL-1 DA_{v1} RELATIVE TO SNOTEL SWE MEASUREMENTS

Snow Period		R [-]	Bias [m]	RMSE [m]	ubRMSE [m]
Accumulation	OL	0.75	-0.10	0.14	0.07
	DA_{v1}	0.81	-0.03*	0.14	0.07
Ablation	OL	0.32	-0.29	0.33	0.11
	DA_{v1}	0.40	-0.22*	0.31	0.13*

Note that the Statistics With an Asterisk Denote Statistically Significant Differences
Between the OL and Sentinel-1 DA_{v1} at a 5% level of significance.

run tends to significantly underestimate snow albedo during the winter. Underestimation of the snow albedo results in an increase of the absorbed radiation and snowmelt, and in turn, reduces the peak snow accumulation. Furthermore, Bosilovich et al. [85] showed that MERRA2 precipitation possesses relatively large error and uncertainties across the Rocky Mountains due to orographic effects related to the complex topography that is not captured in the relatively coarse-scale MERRA2 product. Similarly, Liu and Margulius [86] showed that MERRA2 yielded significantly less snowfall when compared against ensemble-based snowfall reanalyses that more appropriately accounts for uncertainty.

Fig. 3 illustrates the scatter plots of statistical metrics (i.e., bias, RMSE, and ubRMSE) from both Sentinel-1 DA_{v1} and OL versus peak SWE measured from 112 different SNOTEL stations during the study period. Assimilation of C-band backscatter observations into the LSM helped to modestly reduce the magnitude of bias such that the slope of the trend line more closely approaches zero [see Fig. 3(a)]. RMSE and ubRMSE represented in Fig. 3(b) and (c) also showed that Sentinel-1 DA_{v1} yielded slight improvements as the slope of the trend line for Sentinel-1 DA_{v1} is less than that for the OL simulation. However, the statistical evaluation of Sentinel-1 DA_{v1} showed more spread in terms of bias, RMSE, and ubRMSE as a function of peak SWE. In general, the snowpack during the snow accumulation period tends to be dry and shallow. Matzler [87] and Nagler et al. [88] stated that C-band photons travel relatively freely through dry, shallow snowpack with a relatively long penetration depth (∼20 m). As a result, total backscatter measured over dry, shallow snowpack is dominated by backscatter at the snow–land interface rather than due to volume scattering within the snowpack or from backscatter at the air–snow interface. This implies that the total backscatter as observed by Sentinel-1 is dominated by backscatter from the underlying land surface, which is not explicitly considered during SVM training. The lack of this explicit inclusion of information, in part, leads to an increase in random errors when the peak SWE is relatively low.

Domain-averaged statistics of SWE from both the OL and Sentinel-1 DA_{v1} during the snow accumulation period (i.e., December, January, and February) and snow ablation period (i.e., March, April, and May) are summarized in Table II. Overall, statistics during the snow accumulation period showed better

performance than during the snow ablation period. Domain-averaged bias was significantly reduced from −0.10 (OL) to −0.03 m (Sentinel-1 DA_{v1}) and R also revealed a slight improvement from 0.75 (OL) to 0.81 (Sentinel-1 DA_{v1}) yet did not achieve statistically significant differences at the 5% significance level. Even though domain-averaged bias showed significant improvement via Sentinel-1 DA_{v1}, the RMSE and ubRMSE yielded no significant skill differences between the OL and Sentinel-1 DA_{v1}. This behavior is also revealed in Fig. 3(a) in that the bias in Sentinel-1 DA_{v1} showed a relatively wider spread relative to the OL when the peak SWE is less than 0.4 m.

Similar to the snow accumulation period, Sentinel-1 DA_{v1} showed a slight improvement compared to that of the OL during the snow ablation period. More specifically, the ranges of R were −0.17 to 0.93 for the OL and −0.17 to 0.96 for Sentinel-1 DA_{v1}. In the case of bias, the OL yielded a bias range from −0.95 to 0.15 m, while the bias of Sentinel-1 DA_{v1} ranged from −0.62 to 0.20 m. RMSE does not reveal any significant differences between the OL and Sentinel-1 DA_{v1}; ubRMSE showed a slight increase from 0.11 (OL) to 0.13 (Sentinel-1 DA_{v1}) with a statistical significance of 5%. This behavior is likely due to the electromagnetic response of the snowpack to C-band radiation during relatively wet, deep snow conditions. C-band radiation has a much smaller penetration depth during wet snow conditions (∼3 cm) than during dry, shallow snowpack conditions (∼20 m) [67], [89]. This leads C-band backscatter to contain more information related to volume scattering within the snowpack as well as backscatter at the air–snow interface as compared to backscatter at the snow–land interface in the case of dry snow conditions. However, overall statistical metrics were less improved than for the snow accumulation period (see Table II). This reduced improvement is related to the different snowpack properties during the snow ablation period. That is, snowpack during the snow ablation period is likely to have more depth hoar and more internal ice layers. This added complexity in the snowpack introduces a large heterogeneity in terms of electromagnetic response (e.g., absorption and reflection), and in turn, introduces more uncertainty into the predicted backscatter via the SVM as well as estimated SWE via Sentinel-1 DA_{v1}.

B. Influence of Rule-Based Update on Assimilation

Evaluation of SWE estimated from Sentinel-1 DA_{v1} through comparison with ground-based measurements in the previous section revealed that Sentinel-1 DA_{v1} resulted in improving the modeled SWE estimates. This section further investigates the influence of the rule-based updates on the efficacy of Sentinel-1 DA in the context of SVM controllability. More specifically, daily SWE estimates from the Sentinel-1 DA with and without the rule-based update (hereafter denoted as Sentinel-1 DA_{v1} and Sentinel-1 DA_{v2}, respectively) were compared against the ground-based measurements.

Fig. 4 summarizes the domain-averaged R, bias, RMSE, and ubRMSE calculated by comparing SWE estimates from the OL and Sentinel-1 DA simulations, including both DA_{v1} and DA_{v2}, against all available SNOTEL SWE measurements within the study domain. The results confirmed that Sentinel-1 DA_{v1}
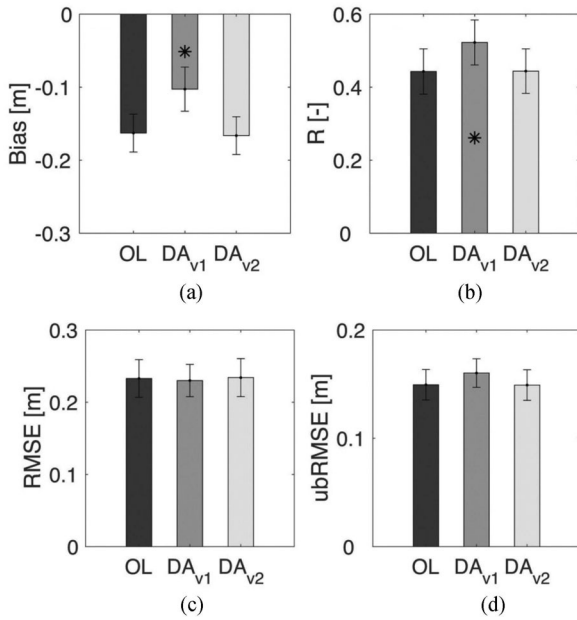
Fig. 4. Domain-averaged goodness-of-fit statistics for SWE simulated from the OL and Sentinel-1 DA (with and without rule-based updates) compared against SNOTEL SWE measurements. DA_{v1} includes the rule-based updates whereas DA_{v2} does not. Error bars represent the 95% confidence interval. Asterisks indicate that the experiment yielded statistically significant differences (relative to the OL) at a 5% significance level.

showed significant improvement in R and bias compared to Sentinel-1 DA_{v2} as well as compared to the OL. For instance, Sentinel-1 DA_{v2} showed no significant difference in terms of domain-averaged bias between the OL [see Fig. 4(a)] while Sentinel-1 DA_{v1} showed a less negative domain averaged bias of -0.11 m. Similarly, OL and Sentinel-1 DA_{v2} did not show a significant difference in R (0.44) while Sentinel-1 DA_{v1} showed a statistically significant level of improvement in terms of temporal agreement with the ground-based measurements [see Fig. 4(b)]. RMSE from the OL and Sentinel-1 DA_{v2} showed a similar range of 0.07–0.66 m, while Sentinel-1 DA_{v1} showed modest improvement from 0.06 to 0.62 m [see Fig. 4(c)]. For the ubRMSE, all three simulations yielded a similar range from 0.04 to 0.38 m.

The spatial distribution of R for the SWE estimates via OL and Sentinel-1 DA_{v2} versus SNOTEL SWE measurements along with their differences in skill are shown in Fig. 5. Among the available SNOTEL stations, 56 sites out of 112 SNOTEL stations yielded better performance in the OL than did Sentinel-1 DA_{v2}. Similar behaviors were observed in terms of bias, RMSE, and ubRMSE in that more than 50% of available stations indicated that the OL performed better than Sentinel-1 DA_{v2}. However, Fig. 5(c) illustrates that the difference in R calculated between Sentinel-1 DA_{v2} and OL against SNOTEL measurements showed that most of the stations indicated no statistically significant improvement in SWE estimates between the OL and Sentinel-1 DA_{v2}. The differences between Fig. 5(c) without the rule-based and Fig. 2(c) with the rule-based update clearly show how incorporating the rule-based update into the DA framework improves the DA performance.

In order to better illustrate the effect of incorporating the rule-based update, the time series of SWE simulated from the OL and Sentinel-1 DA (without and with rule-based updates) at Vail Mountain station [CO 842; represented in Fig. 5(c)] are shown in Fig. 6. Comparing the SWE estimated from the OL and Sentinel-1 DA_{v2}, the results suggest a similar magnitude of SWE between the two. More specifically, R and bias from the OL and Sentinel-1 DA_{v2} showed no statistically significant difference ($< 10^{-3}$) at this specific location. Conversely, SWE estimates from the Sentinel-1 DA_{v1} approach resulted in better agreement with the SNOTEL measurements until early April (see Fig. 6). Statistical metrics also indicated the improvement in terms of R (from 0.70 to 0.84), bias (from -0.12 to 0.07), RMSE (from 0.18 m to 0.12 m), and ubRMSE (from 0.13 m to 0.11 m) in comparison to both the OL and Sentinel-1 DA_{v2}.

The main reason for the difference in performance is due to the different amount of updates associated with the rule-based update approach. At this specific location, predicted σ_{VH} showed reasonable agreement with the observed σ_{VH} while predicted σ_{VV} was heavily biased (deviation larger than -10 dB) compared to the observed σ_{VV} (results not shown). Given the limited number of training data due to a lack of Sentinel-1 observations, SVM regression tends to predict a heavily biased copolarized predicted backscatter at this location. Because Sentinel-1 DA_{v2} used the innovations from both σ_{VV} and σ_{VH} during the update, it yielded a negligible amount of update in terms of SWE. In the case of Sentinel-1 DA_{v1}, on the other hand, because the assimilation switch for σ_{VV} was turned OFF and only σ_{VH} was used in calculating the Kalman gain, the updated SWE had a significantly better agreement with the SNOTEL SWE measurements relative to both the OL and Sentinel-1 DA_{v2} approach. Moreover, another advantage of applying the rule-based update is to further influence the accuracy of predicted backscatter. As the SVM utilizes the updated (*a posterior*) geophysical variables to predict the σ_{VV} and σ_{VH}, it resulted in improving the accuracy of the predicted backscatter and updated SWE during the remainder of the snow season.

C. Evaluation of Modeled River Discharge Against Ground-Based Measurement

Fig. 7 shows the time series of daily averaged river discharge estimates from the OL and Sentinel-1 DA_{v1} simulations at the measurement station located on the North Platte River (northern part of the study domain) from September 2016 to August 2017. Generally speaking, river discharge estimates from both the OL and Sentinel-1 DA_{v1} follow a common seasonal behavior with the measured river discharge in that both Sentinel-1 DA_{v1} and OL yielded a seasonal peak discharge at roughly the same time as the ground-based measurements. More specifically, Fig. 7 highlights small improvements in river discharge during the early runoff season from March through May. This was due to the small, but systematic improvements in the SWE estimates. However, discharge estimates from both the OL and Sentinel-1 DA_{v1} largely underestimated the measurements from late-June to early-July (see Fig. 7). This phenomenon is partly related to
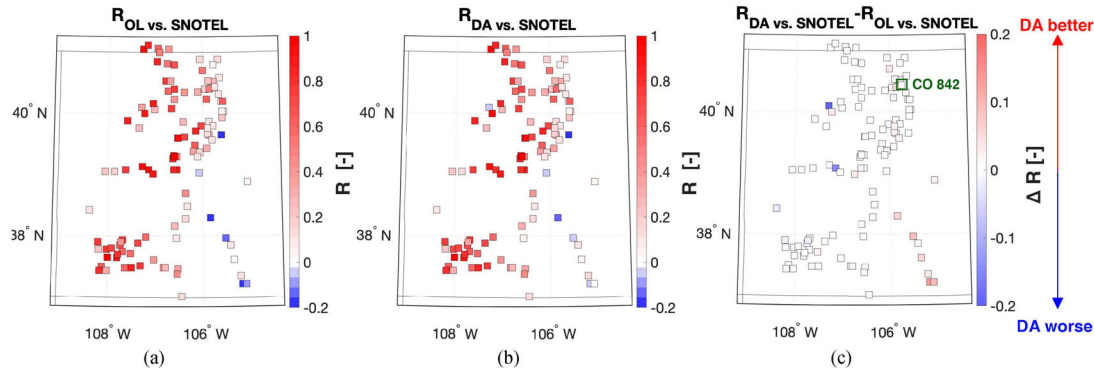
Fig. 5. Spatial maps of the correlation coefficient, R, computed between SNOTEL and (a) OL SWE and (b) Sentinel-1 DA_{v2} (without rule-based update) SWE from September 2016 to August 2017. The difference in *R* between the OL and Sentinel-1 DA_{v2} is shown in (c). The red colors (positive values) in (c) suggests that Sentinel-1 DA_{v2} agrees better with SNOTEL SWE than does the OL. Oppositely, blue colors (negative values) indicate that the OL showed better agreement with SNOTEL SWE than did Sentinel-1 DA_{v2}.
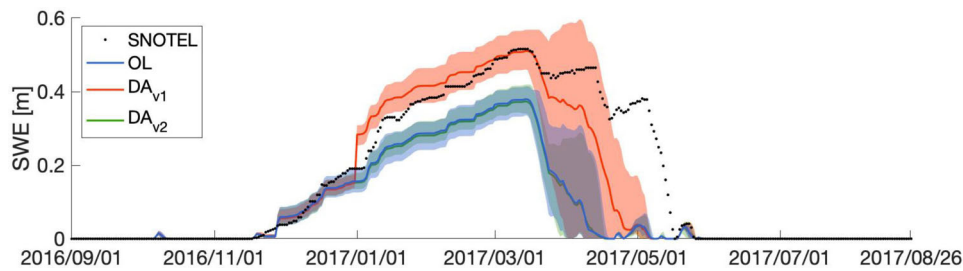
Fig. 6. Time series of SWE estimated from OL (blue) and Sentinel-1 DA with rule-based updates (red) and without rule-based updates (green) along with SNOTEL measurements (black dots) at Vail Mountain station (CO 842; 39.6 °N 106.4 °W). Solid lines represent the ensemble mean of SWE and the corresponding shaded regions represent the ensemble spread of the SWE estimates as ±1 standard deviation.
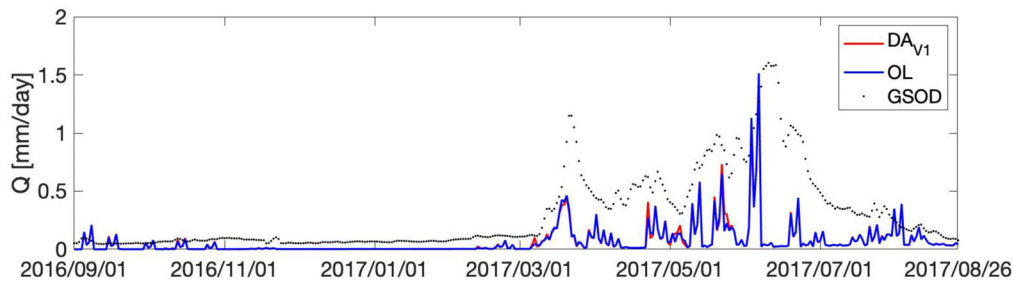

Fig. 7. Time series of river discharge estimated from the OL and Sentinel-1 DA_{v1} relative to ground-based river discharge measurements near Northgate, CO (Station No. 4122154; 40.64 °N 106.34 °W) from September 2016 to August 2017.

errors in meteorological boundary conditions such as precipitation. MERRA-2 precipitation has a relatively coarse spatial resolution that does not accurately capture all of the detailed variations of precipitation over regions with large heterogeneous terrain characteristics. More specifically, precipitation events near the Rockies undergo orographic lifting as mountain barriers force airflow to ascend while coarser-scale precipitation estimates do not fully capture this orographic effect. Bosilovich *et al.* [85] also discussed similar findings that MERRA2 precipitation showed relatively large uncertainties over the Rockies during the summer (e.g., June, July, and August) associated with the complex topography.

Table III highlights the differences in statistical metrics (i.e., bias, RMSE, ubRMSE, and NSE) computed between daily averaged river discharge estimates from the OL and Sentinel-1 DA_{v1}

experiments by comparing against the *in situ* measurements between September 2016 and August 2017. Overall, Sentinel-1 DA_{v1} showed slight improvements in most of the statistics. For example, all eight stations showed improvements in NSE that ranged from 0.29% to 298%, indicating that improved SWE estimates using Sentinel-1 DA_{v1} resulted in improvements in the accuracy of river discharge estimates compared to that of the OL. Similarly, more than 60% of the stations yielded slight improvements in bias, RMSE, and ubRMSE for Sentinel-1 DA_{v1} relative to the OL. However, the comparison of river discharge estimates during the winter period (from December to February) revealed that both the Sentinel-1 DA_{v1} and OL did not produce significant amounts of river discharge. Differences between the simulated and measured river discharge can be explained, in part, by errors and uncertainties in model parameterization.

TABLE III
SUMMARY OF THE DIFFERENCES IN STATISTICS FOR THE OL AND SENTINEL-1 DA$_{v1}$ EXPERIMENTS COMPARED AGAINST
THE *IN SITU* RIVER DISCHARGE MEASUREMENTS WITHIN THE STUDY DOMAIN

Station No.	Drainage Area [$\times 10^2$ km^2]	Δ Bias [$\times 10^2$ mm/day]	Δ RMSE [$\times 10^2$ mm/day]	Δ ubRMSE [$\times 10^2$ mm/day]	Δ NSE [%]
4122154	37.1	0.1	0.1	0	7.1
4151805	34.2	0.2	0.2	0	4.1
4152580	96.6	-1.7	0.4	0.5	298
4152650	146	0.4	0.1	-0.1	1.8
4152651	103	-0.1	0	0.1	0.3
4152652	26.2	0.1	0.1	0.1	2.0
4152700	88.3	4.7	2.7	1.6	16.8
4152701	198	-1.8	-0.5	0.2	10.6

Note that the difference (Δ) of absolute bias, RMSE and ubRMSE were computed as OL versus the observation minus Sentinel-1 DA$_{v1}$ versus observations. The difference (Δ) in NSE was computed in the opposite manner. Positive values of Δ suggest improvements via Sentinel-1 DA$_{v1}$.
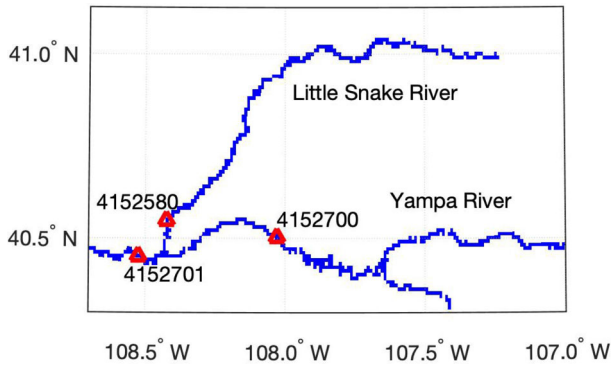

Fig. 8. Maps of the Little Snake River and Yampa River along with the available GRDC stations.

Getirana *et al.* [74] mentioned that an inaccurate representation of the river characteristics (e.g., river width, roughness, and bank height) introduces uncertainty in simulating both streamflow and baseflow.

Among the eight different stations, station 4152700 located on the Yampa River (near Maybell, CO; Fig. 8) showed the largest improvement in terms of bias, RMSE, and ubRMSE (see Table III). The Yampa River is one of the largest free-flowing (i.e., not influenced by upstream dams or water management) rivers, where seasonal variations in river discharge are strongly modulated by snow melt [90]. As a result, updated SWE estimates via Sentinel-1 DA$_{v1}$ resulted in significantly improving the accuracy of river discharge estimates compared to the OL (model-only) run. However, stations 4152580 (near Lily, CO) near and 4152701 (near Deerlodge Park, CO) showed significant increases in bias via Sentinel-1 DA$_{v1}$. These two stations showed similar seasonal behavior in that both the OL and Sentinel-1 DA$_{v1}$ significantly underestimated the river discharge during the summer. One main reason for the high uncertainty at station 4152580 is related to the anthropogenic influence over the Little Snake River. More specifically, river discharge is influenced by the High Savery dam that is located upstream of the measurement location. As human activities (e.g., water management) are not explicitly modeled in Noah-MP, the

poor performance at station 4152580 is likely due to the impact of anthropogenic influences. Furthermore, as the Little Snake River joins the Yampa River near station 4152701, errors and uncertainties present at station 4152580 propagate downstream and subsequently impact the accuracy of river discharge estimates at station 4152701.

V. CONCLUSION

This research is the first attempt to assimilate C-band backscatter observations into an advanced LSM using well-trained SVM regression and ensemble Kalman filtering in order to improve modeled terrestrial SWE. Model experiments (with and without assimilation) were conducted across Western Colorado during the period of September 2016 to August 2017. Evaluation of the SWE estimates from the OL (i.e., without assimilation) as well as from the DA experiments were compared against measurements from 112 SNOTEL stations across the study area. In addition, river discharge modulated by the updated SWE via Sentinel-1 DA was also evaluated by comparing modeled discharge against the available GRDC measurements in the study area.

Prior to evaluating the performance of the DA algorithm, the influence of applying a rule-based update that served as a quality control constraint was evaluated by comparing SWE estimates from DA (with and without the rule-based update) against SNOTEL SWE measurements. In general, more than 50% of the SNOTEL stations yielded marginal improvements in terms of R and bias; however, many of these improvements were near-zero and not statistically pronounced. When constraints on the range of predicted backscatter, $\hat{\sigma}^0_{VV}$ and $\hat{\sigma}^0_{VH}$, were introduced using the rule-based update, the improvements were much more pronounced. The rule-based update helped mitigate some of the SVM controllability issues related to sparse training datasets. Furthermore, the application of the rule-based update also influenced the accuracy of SVM-based predicted backscatter, and in turn, positively influenced the overall accuracy of the SWE updates via assimilation.

A detailed assessment of SWE estimates from Sentinel-1 DA$_{v1}$ (with the rule-based update) showed the capability of

Sentinel-1 DA_{v1} to improve the accuracy of SWE estimates relative to the OL. More specifically, Sentinel-1 DA_{v1} yielded improvements at more than 75% of the SNOTEL stations (relative to the OL) in terms of bias and R. Computed bias showed statistically significant improvements during both the snow accumulation (e.g. -0.10 m [OL] to -0.03 m [Sentinel-1 DA_{v1}]) and snow ablation periods (e.g. -0.29 m [OL] to -0.22 m [Sentinel-1 DA_{v1}]). In the case of RMSE and ubRMSE, there were no statistically significant differences between the OL and Sentinel-1 DA_{v1} even though ubRMSE was slightly increased when using Sentinel-1 DA_{v1}. In addition, bias, RMSE, and ubRMSE from Sentinel-1 DA_{v1} showed more uncertainty (statistical spread) when SWE measured by SNOTEL was relatively small, which is partly related to the relatively small sensitivity of C-band backscatter during dry, shallow snow conditions.

Evaluation of updated river discharge estimates using the HyMAP river routing scheme in conjunction with Sentinel-1 DA_{v1} also yielded slight improvements over that of the OL when compared against the *in situ* river discharge measurements provided by GRDC. More specifically, all the available stations yielded improvements in Nash-Sutcliffe model efficiency (NSE) when using Sentinel-1 DA_{v1}. Sentinel-1 DA_{v1} also showed some advantages in small improvements in the magnitude of the peak river discharge early in the spring runoff season. Additionally, more than 60% of the stations yielded improvements in terms of bias, RMSE, and ubRMSE. Despite these improvements, more work is needed to further improve the HyMAP parameterizations of river geometry as well as bathymetric elevation, which is highly related to the accurate representation of floodplains and reservoirs that in turn dictates much of the computed streamflow and baseflow.

In summary, this study presented a new and novel use of C-band backscatter observations to improve model estimates of terrestrial SWE. Results demonstrated the capability of SVM regression to be used as an observation operator within a C-band backscatter assimilation framework in order to improve the characterization of snow mass. Furthermore, a rule-based update implemented as part of the Sentinel-1 DA routine helped mitigate some of the controllability issues of SVM regression when trained with a sparse training dataset. The improvement in SWE estimates from Sentinel-1 DA, when compared against SNOTEL SWE measurements, demonstrated some of the utility in using C-band backscatter observations to improve modeled terrestrial snow mass, and in turn, resulted in slight improvements in modeled river discharge. This research further motivates the application of physically constrained SVM regression that more appropriately (and explicitly) considers the first-order physics of the electromagnetic response of terrestrial snow to C-band SAR. As a next step, consideration of the ratio of cross- and co-polarized backscatter instead of individual backscatter coefficient should be considered in the future C-band DA frameworks in order to maximize the sensitivity of backscatter toward snow mass information. Furthermore, exploration of the joint assimilation of C-band backscatter in conjunction with other types of snow-related observation, heuristic assimilation based on *a priori* snow conditions, and careful consideration of spatially variant observation error is recommended for future study.

REFERENCES

[1] A. R. Hedrick *et al.*, "Direct insertion of NASA airborne snow observatory-derived snow depth time series into the Isnobal energy balance snow model," *Water Resour. Res.*, vol. 54, no. 10, pp. 8045–8063, 2018. [Online]. Available: https://agupubs.onlinelibrary.wiley.com/doi/abs/10.1029/2018WR023190

[2] H. Lievens *et al.*, "Snow depth variability in the northern hemisphere mountains observed from space," *Nature Commun.*, vol. 10, no. 1, pp. 1–12, 2019.

[3] T. E. Shaw, S. Gascoin, P. A. Mendoza, F. Pellicciotti, and J. McPhee, "Snow depth patterns in a high mountain Andean catchment from satellite optical tristereoscopic remote sensing," *Water Resour. Res.*, vol. 56, no. 2, 2020, Art. no. e2019WR024880. [Online]. Available: https://agupubs.onlinelibrary.wiley.com/doi/abs/10.1029/2019WR024880

[4] C. Mortimer *et al.*, "Evaluation of long-term northern hemisphere snow water equivalent products," *Cryosphere*, vol. 14, no. 5, pp. 1579–1594, 2020. [Online]. Available: https://tc.copernicus.org/articles/14/1579/2020/

[5] Y. Xue, B. A. Forman, and R. H. Reichle, "Estimating snow mass in north america through assimilation of advanced microwave scanning radiometer brightness temperature observations using the catchment land surface model and support vector machines," *Water Resour. Res.*, vol. 54, no. 9, pp. 6488–6509, 2018.

[6] G. J. De Lannoy and R. Reichle, "Assimilation of SMOS brightness temperatures or soil moisture retrievals into a land surface model," *Hydrol. Earth Syst. Sci.*, vol. 20, no. 12, pp. 4895–4911, 2016.

[7] D. Günther, T. Marke, R. Essery, and U. Strasser, "Uncertainties in snowpack simulations-assessing the impact of model structure, parameter choice, and forcing data error on point-scale energy balance snow model performance," *Water Resour. Res.*, vol. 55, no. 4, pp. 2779–2800, 2019.

[8] A. Chang, J. Foster, D. Hall, A. Rango, and B. Hartline, "Snow water equivalent estimation by microwave radiometry," *Cold Regions Sci. Technol.*, vol. 5, no. 3, pp. 259–267, 1982.

[9] A. Chang, J. Foster, and D. Hall, "Nimbus-7 SMMR derived global snow cover parameters," *Ann. Glaciol.*, vol. 9, pp. 39–44, 1987.

[10] A. W. Nolin, "Recent advances in remote sensing of seasonal snow," *J. Glaciol.*, vol. 56, no. 200, pp. 1141–1150, 2010.

[11] J. L. Foster *et al.*, "Quantifying the uncertainty in passive microwave snow water equivalent observations," *Remote Sens. Environ.*, vol. 94, no. 2, pp. 187–203, 2005.

[12] M. Tedesco and P. S. Narvekar, "Assessment of the NASA AMSR-E SWE product," *IEEE J. Sel. Topics Appl. Earth Observ. Remote Sens.*, vol. 3, no. 1, pp. 141–159, Mar. 2010.

[13] F. T. Ulaby, W. H. Stiles, L. F. Dellwig, and B. C. Hanson, "Experiments on the radar backscatter of snow," *IEEE Trans. Geosci. Electron.*, vol. 15, no. 4, pp. 185–189, Oct. 1977.

[14] P. Thakur, P. Grag, S. Aggarwal, R. Garg, and S. Mani, "Snow cover area mapping using synthetic aperture radar in Manali watershed of Beas river in the northwest himalayas," *J. Indian Soc. Remote Sens.*, vol. 41, no. 4, pp. 933–945, 2013.

[15] J. Shi and J. Dozier, "Estimation of snow water equivalence using SIR-C/X-SAR. Inferring snow density and subsurface properties," *IEEE Trans. Geosci. Remote Sens.*, vol. 38, no. 6, pp. 2465–2474, Nov. 2000.

[16] T. Guneriussen, K. A. Hogda, H. Johnsen, and I. Lauknes, "InSAR for estimation of changes in snow water equivalent of dry snow," *IEEE Trans. Geosci. Remote Sens.*, vol. 39, no. 10, pp. 2101–2108, Oct. 2001.

[17] H. Li, Z. Wang, G. He, and W. Man, "Estimating snow depth and snow water equivalence using repeat-pass interferometric SAR in the northern Piedmont region of the Tianshan mountains," *J. Sensors*, vol. 2017, 2017, Art. no. 8739598.

[18] M. Bernier, J.-P. Fortin, Y. Gauthier, R. Gauthier, R. Roy, and P. Vincent, "Determination of snow water equivalent using Radarsat SAR data in eastern Canada," *Hydrological Process.*, vol. 13, no. 18, pp. 3041–3051, 1999.

[19] V. Conde, G. Nico, P. Mateus, J. Catalão, A. Kontu, and M. Gritsevich, "On the estimation of temporal changes of snow water equivalent by Spaceborne SAR interferometry: A new application for the sentinel-1 mission," *J. Hydrol. Hydromechanics*, vol. 67, no. 1, pp. 93–100, 2019.

[20] S. Sun *et al.*, "Estimation and analysis of snow water equivalents based on C-band SAR data and field measurements," *Arctic, Antarctic, Alpine Res.*, vol. 47, no. 2, pp. 313–326, 2015.

[21] R. Reichle, "Data assimilation methods in the earth sciences," *Adv. Water Resour.*, vol. 31, no. 11, pp. 1411–1418, 2008.

[22] K. M. Andreadis and D. P. Lettenmaier, "Assimilating remotely sensed snow observations into a macroscale hydrology model," *Adv. Water Resour.*, vol. 29, no. 6, pp. 872–886, 2006.

[23] G. J. De Lannoy *et al.*, "Multiscale assimilation of advanced microwave scanning radiometer-EOS snow water equivalent and moderate resolution imaging spectroradiometer snow cover fraction observations in Northern Colorado," *Water Resour. Res.*, vol. 48, no. 1, pp. 1–17, 2012.

[24] K. R. Arsenault, P. R. Houser, G. J. M. De Lannoy, and P. A. Dirmeyer, "Impacts of snow cover fraction data assimilation on modeled energy and moisture budgets," *J. Geophys. Res., Atmos.*, vol. 118, no. 14, pp. 7489–7504, 2013.

[25] S. A. Margulis, M. Girotto, G. Cortés, and M. Durand, "A particle batch smoother approach to snow water equivalent estimation," *J. Hydrometeorol.*, vol. 16, no. 4, pp. 1752–1772, 2015.

[26] C. M. Oaida *et al.*, "A high-resolution data assimilation framework for snow water equivalent estimation across the western United States and validation with the airborne snow observatory," *J. Hydrometeorol.*, vol. 20, no. 3, pp. 357–378, 2019.

[27] J. Pulliainen, "Mapping of snow water equivalent and snow depth in boreal and sub-arctic zones by assimilating space-borne microwave radiometer data and ground-based observations," *Remote Sens. Environ.*, vol. 101, no. 2, pp. 257–269, 2006.

[28] C. Dechant and H. Moradkhani, "Radiance data assimilation for operational snow and streamflow forecasting," *Adv. Water Resour.*, vol. 34, no. 3, pp. 351–364, 2011.

[29] F. Larue, A. Royer, D. De Sève, A. Roy, and E. Cosme, "Assimilation of passive microwave AMSR-2 satellite observations in a snowpack evolution model over northeastern Canada," *Hydrol. Earth Syst. Sci.*, vol. 22, no. 11, pp. 5711–5734, 2018.

[30] M. Takala *et al.*, "Estimating northern hemisphere snow water equivalent for climate research through assimilation of space-borne radiometer data and ground-based measurements," *Remote Sens. Environ.*, vol. 115, no. 12, pp. 3517–3529, 2011.

[31] K. M. Andreadis and D. P. Lettenmaier, "Implications of representing snowpack stratigraphy for the assimilation of passive microwave satellite observations," *J. Hydrometeorol.*, vol. 13, no. 5, pp. 1493–1506, 2012.

[32] S. V. Kumar *et al.*, "Assimilation of remotely sensed soil moisture and snow depth retrievals for drought estimation," *J. Hydrometeorol.*, vol. 15, no. 6, pp. 2446–2469, 2014.

[33] K. P. Luojus, J. T. Pulliainen, S. J. Metsamaki, and M. T. Hallikainen, "Enhanced SAR-based snow-covered area estimation method for Boreal forest zone," *IEEE Trans. Geosci. Remote Sens.*, vol. 47, no. 3, pp. 922–935, Mar. 2009.

[34] X. V. Phan *et al.*, "1D-VAR multilayer assimilation of X-band SAR data into a detailed snowpack model," *Cryosphere*, vol. 8, no. 5, pp. 1975–1987, 2014.

[35] R. Reichle, G. J. De Lannoy, B. A. Forman, C. S. Draper, and Q. Liu, "Connecting satellite observations with water cycle variables through land data assimilation: Examples using the NASA GEOS-5 LDAS," *Surv. Geophys.*, vol. 35, no. 3, pp. 577–606, 2014.

[36] J. A. Ahmad, B. A. Forman, and Y. Kwon, "Analyzing machine learning predictions of passive microwave brightness temperature spectral difference over snow-covered terrain in high mountain Asia," *Front. Earth Sci.*, vol. 7, 2019, Art. no. 212.

[37] B. A. Forman, R. H. Reichle, and C. Derksen, "Estimating passive microwave brightness temperature over snow-covered land in north America using a land surface model and an artificial neural network," *IEEE Trans. Geosci. Remote Sens.*, vol. 52, no. 1, pp. 235–248, Jan. 2014.

[38] B. A. Forman and Y. Xue, "Machine learning predictions of passive microwave brightness temperature over snow-covered land using the special sensor microwave imager (SSM/I)," *Phys. Geogr.*, vol. 38, no. 2, pp. 176–196, 2017.

[39] Y. Kwon, B. A. Forman, J. A. Ahmad, S. V. Kumar, and Y. Yoon, "Exploring the utility of machine learning-based passive microwave brightness temperature data assimilation over terrestrial snow in high mountain Asia," *Remote Sens.*, vol. 11, no. 19, 2019, Art. no. 2265. [Online]. Available: https://www.mdpi.com/2072-4292/11/19/2265

[40] J. Park, B. A. Forman, and H. Lievens, "Prediction of active microwave backscatter over snow-covered terrain across Western Colorado using a land surface model and support vector machine regression," *IEEE J. Sel. Topics Appl. Earth Observ. Remote Sens.*, vol. 14, pp. 2403–2417, 2021, doi: 10.1109/JSTARS.2021.3053945.

[41] J. A. Vano *et al.*, "Understanding uncertainties in future Colorado river streamflow," *Bull. Amer. Meteorological Soc.*, vol. 95, no. 1, pp. 59–78, 2014.

[42] D. L. Ficklin, I. T. Stewart, and E. P. Maurer, "Climate change impacts on streamflow and Subbasin-scale hydrology in the Upper Colorado river basin," *PLoS One*, vol. 8, no. 8, 2013, Art. no. e71297.

[43] N. Salzmann and L. O. Mearns, "Assessing the performance of multiple regional climate model simulations for seasonal mountain snow in the Upper Colorado River Basin," *J. Hydrometeorol.*, vol. 13, no. 2, pp. 539–556, 2012.

[44] N. S. Christensen, A. W. Wood, N. Voisin, D. P. Lettenmaier, and R. N. Palmer, "The effects of climate change on the hydrology and water resources of the Colorado River Basin," *Climatic Change*, vol. 62, nos. 1–3, pp. 337–363, 2004.

[45] J. Aschbacher and M. P. Milagro-Peréz, "The European Earth monitoring (GMES) programme: Status and perspectives," *Remote Sens. Environ.*, vol. 120, pp. 3–8, 2012.

[46] R. Torres *et al.*, "GMES sentinel-1 mission," *Remote Sens. Environ.*, vol. 120, pp. 9–24, 2012.

[47] R. S. Caprari, A. S. Goh, and E. K. Moffatt, "Noise and speckle reduction in synthetic aperture radar imagery by nonparametric wiener filtering," *Appl. Opt.*, vol. 39, no. 35, pp. 6633–6640, 2000.

[48] S. Kumar *et al.*, "Land information system: An interoperable framework for high resolution land surface modeling," *Environ. Modelling Softw.*, vol. 21, no. 10, pp. 1402–1415, 2006.

[49] G.-Y. Niu *et al.*, "The community Noah land surface model with multi-parameterization options (NOAH-MP): 1. Model description and evaluation with local-scale measurements," *J. Geophys. Res., Atmos.*, vol. 116, no. D12, 2011, doi: 10.1029/2010JD015139.

[50] Z.-L. Yang *et al.*, "The community Noah land surface model with multiparameterization options (NOAH-MP): 2 Evaluation over global river basins," *J. Geophys. Res., Atmos.*, vol. 116, no. D12, 2011, doi: 10.1029/2010JD015140.

[51] Z.-L. Yang and R. E. Dickinson, "Description of the biosphere-atmosphere transfer scheme (bats) for the soil moisture workshop and evaluation of its performance," *Glob. Planet. Change*, vol. 13, nos. 1–4, pp. 117–134, 1996.

[52] R. E. Jordan, "A one-dimensional temperature model for a snow cover: Technical documentation for SNTHERM 89," U.S. Army Cold Regions Res. Eng. Lab., Special Rep. 91-16, p. 49, 1991.

[53] R. Gelaro *et al.*, "The modern-era retrospective analysis for research and applications, version 2 (merra-2)," *J. Climate*, vol. 30, no. 14, pp. 5419–5454, 2017.

[54] G. J. Huffman *et al.*, "The trmm multisatellite precipitation analysis (TMPA): Quasi-global, multiyear, combined-sensor precipitation estimates at fine scales," *J. Hydrometeorol.*, vol. 8, no. 1, pp. 38–55, 2007.

[55] G. Evensen, "The ensemble Kalman filter: Theoretical formulation and practical implementation," *Ocean Dyn.*, vol. 53, no. 4, pp. 343–367, 2003.

[56] C. Huang, X. Li, L. Lu, and J. Gu, "Experiments of one-dimensional soil moisture assimilation system based on ensemble Kalman filter," *Remote Sens. Environ.*, vol. 112, no. 3, pp. 888–900, 2008.

[57] R. Reichle, D. B. McLaughlin, and D. Entekhabi, "Hydrologic data assimilation with the ensemble Kalman filter," *J. Hydrometeorol.*, vol. 130, pp. 103–114, 2002.

[58] A. Gruber, G. De Lannoy, and W. Crow, "A Monte Carlo based adaptive Kalman filtering framework for soil moisture data assimilation," *Remote Sens. Environ.*, vol. 228, pp. 105–114, 2019.

[59] A. G. Slater and M. P. Clark, "Snow data assimilation via an ensemble Kalman filter," *J. Hydrometeorol.*, vol. 7, no. 3, pp. 478–493, 2006.

[60] G. J. De Lannoy, R. H. Reichle, P. R. Houser, K. R. Arsenault, N. E. Verhoest, and V. R. Pauwels, "Satellite-scale snow water equivalent assimilation into a high-resolution land surface model," *J. Hydrometeorol.*, vol. 11, no. 2, pp. 352–369, 2010.

[61] C. Garnaud *et al.*, "Quantifying snow mass mission concept trade-offs using an observing system simulation experiment," *J. Hydrometeorol.*, vol. 20, no. 1, pp. 155–173, 2019.

[62] M. P. Clark *et al.*, "Hydrological data assimilation with the ensemble Kalman filter: Use of streamflow observations to update states in a distributed hydrological model," *Adv. Water Resour.*, vol. 31, no. 10, pp. 1309–1324, 2008.

[63] T. Z. Gichamo and D. G. Tarboton, "Ensemble streamflow forecasting using an energy balance snowmelt model coupled to a distributed hydrologic model with assimilation of snow and streamflow observations," *Water Resour. Res.*, vol. 55, no. 12, pp. 10813–10838, 2019.

[64] H. Lievens *et al.*, "Joint sentinel-1 and SMAP data assimilation to improve soil moisture estimates," *Geophysical Res. Lett.*, vol. 44, no. 12, pp. 6145–6153, 2017.

[65] B. A. Forman and R. H. Reichle, "Using a support vector machine and a land surface model to estimate large-scale passive microwave brightness temperatures over snow-covered land in North America," *IEEE J. Sel. Topics Appl. Earth Observ. Remote Sens.*, vol. 8, no. 9, pp. 4431–4441, Sep. 2015.

[66] C.-C. Chang and C.-J. Lin, "LIBSVM: A library for support vector machines," *ACM Trans. Intell. Syst. Technol.*, vol. 2, no. 3, 2011, Art. no. 27.

[67] F. T. Ulaby, R. K. Moore, and A. K. Fung, *Microwave Remote Sensing: Active and Passive. Volume 3-From Theory to Applications*. Reading, MA, USA: Addison-Wesley, 1986.

[68] J. Shi and J. Dozier, "Radar backscattering response to wet snow," in *Proc. Int. Geosci. Remote Sens. Symp.*, vol. 2, 1992, pp. 927–929.

[69] J. Shi, R. E. Davis, and J. Dozier, "Stereological determination of dry-snow parameters for discrete-scatterer microwave modeling," *Ann. Glaciol.*, vol. 17, pp. 295–299, 1993.

[70] S. Liang, *Advances in Land Remote Sensing: System, Modeling, Inversion and Application*. Berlin, Germany: Springer, ch. 3.3, 2008.

[71] J. Du, J. Shi, and H. Rott, "Comparison between a multi-scattering and multi-layer snow scattering model and its parameterized snow backscattering model," *Remote Sens. Environ.*, vol. 114, no. 5, pp. 1089–1098, 2010.

[72] S. H. Yueh, S. J. Dinardo, A. Akgiray, R. West, D. W. Cline, and K. Elder, "Airborne Ku-band polarimetric radar remote sensing of terrestrial snow cover," *IEEE Trans. Geosci. Remote Sens.*, vol. 47, no. 10, pp. 3347–3364, Oct. 2009.

[73] C.-C. Tsui, *Robust Control System Design: Advanced State Space Techniques*. Boca Raton, FL, USA: CRC Press, ch. 1.3, 2003.

[74] A. Getirana, A. Boone, D. Yamazaki, B. Decharme, F. Papa, and N. Mognard, "The hydrological modeling and analysis platform (HYMAP): Evaluation in the Amazon Basin," *J. Hydrometeorol.*, vol. 13, no. 6, pp. 1641–1665, 2012.

[75] A. Getirana *et al.*, "Water balance in the Amazon Basin from a land surface model ensemble," *J. Hydrometeorol.*, vol. 15, no. 6, pp. 2586–2614, 2014.

[76] A. Getirana, S. Kumar, M. Girotto, and M. Rodell, "Rivers and floodplains as key components of global terrestrial water storage variability," *Geophysical Res. Lett.*, vol. 44, no. 20, pp. 10359–10368, 2017.

[77] A. Getirana *et al.*, "Satellite gravimetry improves seasonal streamflow forecast initialization in Africa," *Water Resour. Res.*, vol. 56, no. 2, 2020, Art. no. e2019WR026259.

[78] H. C. Jung *et al.*, "Upper Blue Nile Basin water budget from a multi-model perspective," *J. Hydrol.*, vol. 555, pp. 535–546, 2017.

[79] A. McNally *et al.*, "Acute water-scarcity monitoring for Africa," *Water*, vol. 11, no. 10, 2019, Art. no. 1968.

[80] A. M. Toure, K. Luojus, M. Rodell, H. Beaudoing, and A. Getirana, "Evaluation of simulated snow and snowmelt timing in the community land model using satellite-based products and streamflow observations," *J. Adv. Model. Earth Syst.*, vol. 10, no. 11, pp. 2933–2951, 2018.

[81] D. Entekhabi, R. H. Reichle, R. D. Koster, and W. T. Crow, "Performance metrics for soil moisture retrievals and application requirements," *J. Hydrometeorol.*, vol. 11, no. 3, pp. 832–840, Jun. 2010.

[82] J. E. Nash and J. V. Sutcliffe, "River flow forecasting through conceptual models Part I-A discussion of principles," *J. Hydrol.*, vol. 10, no. 3, pp. 282–290, 1970.

[83] E. H. Bair, K. Rittger, S. M. Skiles, and J. Dozier, "An examination of snow albedo estimates from Modis and their impact on snow water equivalent reconstruction," *Water Resour. Res.*, vol. 55, no. 9, pp. 7826–7842, 2019.

[84] S. Kumar, D. Mocko, C. Vuyovich, and C. Peters-Lidard, "Impact of surface albedo assimilation on snow estimation," *Remote Sens.*, vol. 12, no. 4, 2020, Art. no. 645. [Online]. Available: https://www.mdpi.com/2072-4292/12/4/645

[85] M. G. Bosilovich *et al.*, "MERRA-2: Initial evaluation of the climate," *Tech. Rep. Ser. Global Modeling Data Assimilation*, vol. 43, 2015.

[86] Y. Liu and S. A. Margulis, "Deriving bias and uncertainty in MERRA-2 snowfall precipitation over high mountain Asia," *Front. Earth Sci.*, vol. 7, 2019, Art. no. 280.

[87] C. Mätzler, "Applications of the interaction of microwaves with the natural snow cover," *Remote Sens. Rev.*, vol. 2, no. 2, pp. 259–387, 1987.

[88] T. Nagler, H. Rott, E. Ripper, G. Bippus, and M. Hetzenecker, "Advancements for snowmelt monitoring by means of sentinel-1 SAR," *Remote Sens.*, vol. 8, no. 4, 2016, Art. no. 348. [Online]. Available: https://doi.org/10.3390/rs8040348

[89] Y.-L. S. Tsai, A. Dietz, N. Oppelt, and C. Kuenzer, "Wet and dry snow detection using sentinel-1 SAR data for mountainous areas with a machine learning technique," *Remote Sens.*, vol. 11, no. 8, 2019, Art. no. 895. [Online]. Available: https://doi.org/10.3390/rs11080895

[90] L. E. Hay, G. H. Leavesley, M. P. Clark, S. L. Markstrom, R. J. Viger, and M. Umemoto, "Step wise, multiple objective calibration of a hydrologic model for a snowmelt dominated basin 1," *JAWRA J. Amer. Water Resour. Assoc.*, vol. 42, no. 4, pp. 877–890, 2006.

Jongmin Park received the B.S. in civil and environmental engineering from Hanyang University, Seoul, South Korea, in 2014, the M.S. degree in water resources engineering from the Sungkyunkwan University, Suwon, South Korea, in 2016, and the Ph.D degree in civil and environmental engineering from University of Maryland at College Park, MD, USA, in 2020.

Currently, he is a visiting Post-Doctoral Researcher with the Goddard Earth Sciences Technology and Research (GESTER), Universities Space Research Association and Global Modeling and Assimilation Office (GMAO) of NASA Goddard Space Flight Center. His research interests include the application of remote sensing, machine learning, and data assimilation in the context of terrestrial hydrology.

Barton A. Forman received the B.S. (*cum laude*) degree in civil engineering from the University of Virginia, Charlottesville, VA, USA, in 1998, the M.S. degree in civil and environmental engineering from the University of California at Berkeley, Berkeley, CA, USA, in 1999, and the Ph.D. degree in civil engineering from the University of California at Los Angeles, Los Angeles, CA, USA, in 2010.

He is currently an Associate Professor with the Department of Civil and Environmental Engineering, University of Maryland, College Park, MD, USA. His research interests include estimation of snowpack using space-based measurements of the Earth's gravitational field as well as high-performance computing applications related to terrestrial hydrology.

Sujay V. Kumar received the B.Tech degree in civil engineering from the Indian Institute of Technology, Bombay, India, in 1996, the M.S. degree in civil engineering from the North Carolina State University, Raleigh, NC, USA, in 1998, and the Ph.D. degree in civil engineering from the North Carolina State University, Raleigh, in 2002.

He is currently with the Hydrological Science laboratory, Goddard Space Flight Center, National Aeronautics and Space Administration, Greenbelt, MD, USA. His research interests include e terrestrial hydrology, remote sensing data assimilation, high-performance computing, and Earth system modeling.